

Endless Dirac nodal lines and high mobility in kagome semimetal $\text{Ni}_3\text{In}_2\text{Se}_2$ single crystal

Sanand Kumar Pradhan,¹ Sharadnarayan Pradhan,¹ Priyanath Mal,² P. Rambabu,¹ Archana Lakhani,³ Bipul Das,⁴ Bheema Lingam Chittari,⁵ G. R. Turpu,¹ and Pradip Das^{1, a)}

¹⁾Department of Pure and Applied Physics, Guru Ghasidas Vishwavidyalaya, Koni, Bilaspur-495009, C. G., India.

²⁾Department of Physics and Photon Science, Gwangju Institute of Science and Technology (GIST), Gwangju 61005, Republic of Korea.

³⁾UGC-DAE CSR, University Campus, Khandwa Road, Indore, 452001, India.

⁴⁾Department of Physics, National Taiwan Normal University, 162, Section 1, Heping E. Rd., Taipei City 106, Taiwan.

⁵⁾Department of Physical Sciences, Indian Institute of Science Education and Research Kolkata, Mohanpur 741246, West Bengal, India.

(Dated: 9 January 2024)

Kagome-lattice crystal is crucial in quantum materials research, exhibiting unique transport properties due to its rich band structure and the presence of nodal lines and rings. Here, we investigate the electronic transport properties and perform first-principles calculations for $\text{Ni}_3\text{In}_2\text{Se}_2$ kagome topological semimetal. First-principle calculations indicate six endless Dirac nodal lines and two nodal rings with a π -Berry phase in the $\text{Ni}_3\text{In}_2\text{Se}_2$ compound. The temperature-dependent resistivity is dominated by two scattering mechanisms: s - d interband scattering occurs below 50 K, while electron-phonon (e - p) scattering is observed above 50 K. The magnetoresistance (MR) curve aligns with the theory of extended Kohler's rule, suggesting multiple scattering origins and temperature-dependent carrier densities. A maximum MR of 120% at 2 K and 9 T, with a maximum estimated mobility of approximately $3000 \text{ cm}^2\text{V}^{-1}\text{s}^{-1}$ are observed. The Ni atom's hole-like $d_{x^2-y^2}$ and electron-like d_{z^2} orbitals exhibit peaks and valleys, forming a local indirect-type band gap near the Fermi level (E_F). This configuration enhances the motion of electrons and holes, resulting in high mobility and relatively high magnetoresistance.

In recent years, kagome-lattice crystals, especially metals, have gained attention for potential applications in electronics and spintronics. Kagome metals, with a frustrated sub-lattice, explore many exquisite quantum phenomena, including quantum Hall systems at low temperatures, strongly correlated materials, ferromagnetic quantum materials, and topological materials.¹⁻¹¹ Theoretical models unveil nontrivial quantum interference, producing features like flat bands and Dirac fermions. Multi-band studies near the Fermi level reveal potential topological nodal lines, seen in ferromagnetic shandite kagome-metal $\text{Co}_3\text{Sn}_2\text{S}_2$,¹²⁻¹⁵ where the nodal ring transforms into Weyl nodes under strong spin-orbit coupling (SOC), with intrinsic Berry curvature contributing to a large anomalous Hall angle and giant anomalous Hall effect.¹⁶⁻¹⁹ A nonmagnetic counterpart shandite compound $\text{Ni}_3\text{In}_2\text{S}_2$ reveal a novel feature of endless Dirac nodal line by angle-resolved photoemission spectroscopy (ARPES) and density functional theory (DFT) calculations.²⁰ In $\text{Ni}_3\text{In}_2\text{S}_2$, the SOC can be marginally increased by substituting Se at the S site in the kagome lattice, without affecting the magnetic contributions. According to recent literature, $\text{Ni}_3\text{In}_2\text{Se}_2$ is identified as a multi-band topological semimetal, showcasing a MR of 70% and a mobility of $1000 \text{ cm}^2\text{V}^{-1}\text{s}^{-1}$.²¹ However, neither ARPES nor DFT calculations have reported the existence of endless Dirac nodal lines in this compound. Additionally, en-

hancing the mobility is crucial for the practical application of kagome materials in high-mobility electronic devices.

Here, we present the endless Dirac nodal lines and nodal rings based on DFT calculations in a high quality kagome lattice of $\text{Ni}_3\text{In}_2\text{Se}_2$. Experimental electronic transport properties reveal the $\text{Ni}_3\text{In}_2\text{Se}_2$ is an electron-hole (e - h) compensated semimetal with high mobility $\sim 3000 \text{ cm}^2\text{V}^{-1}\text{s}^{-1}$ and MR 120% at 2 K. The electron-like $d_{x^2-y^2}$ and hole-like d_{z^2} orbitals of Ni contribute to peaks and valleys in the electronic band structure, forming a local indirect type band gap near the Fermi level (E_F). This configuration accelerates the electron and hole motion and resulting in high mobility and MR. Two distinct scattering mechanisms, e - p scattering above 50 K and s - d interband scattering below 50 K, dominate the temperature-dependent resistivity. Unlike, the recent report where only one type of scattering mechanism is responsible for evolution of resistivity with temperatures.²¹ The MR curves follow extended Kohler's rule, suggesting a temperature-dependent carrier density variations rather than the ordinary Kohler's rule.

The single crystal of $\text{Ni}_3\text{In}_2\text{Se}_2$ was grown using a modified Bridgman technique. The crystal growth process involved using high-purity starting materials are Nickel powder (99.99% purity), Indium pieces (99.99% purity), and Selenium powder (99.99% purity), which were double-sealed in an evacuated quartz tube under an argon atmosphere. The sealed tube was heated to 1323 K and slowly cooled to 773 K at a rate of 2 K/h. X-ray diffraction analysis for polycrystalline and single crys-

^{a)}Electronic mail: pradip.iitb@gmail.com

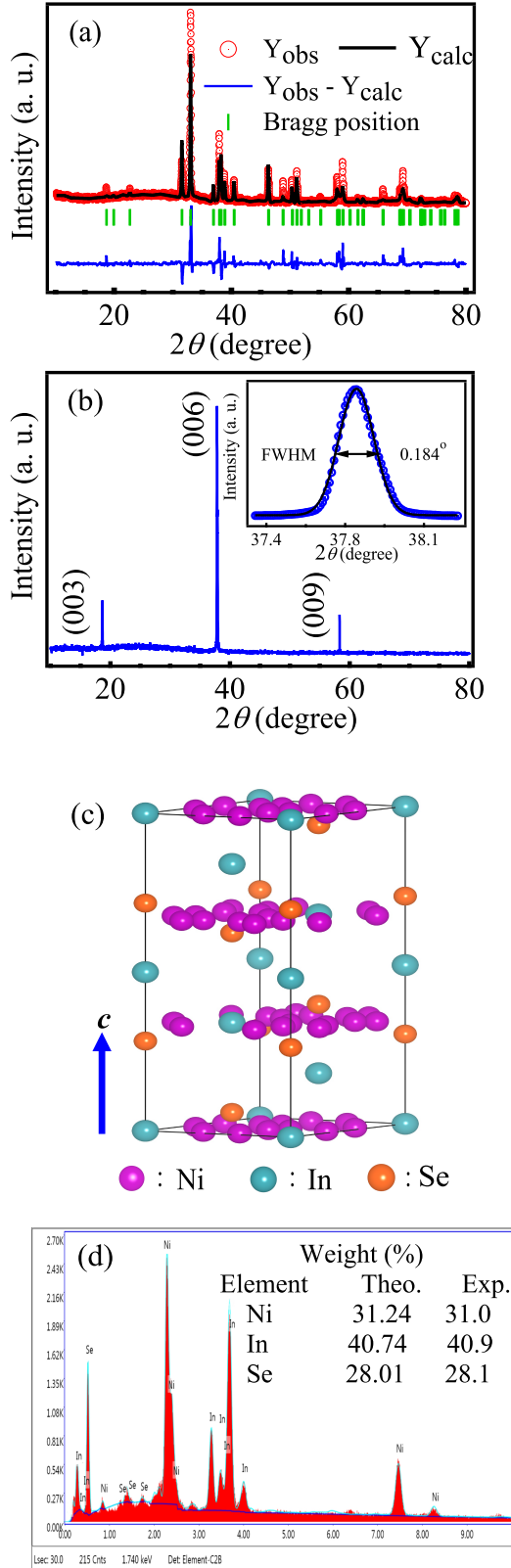


FIG. 1. (a) Rietveld refinement of room temperature polycrystalline x-ray diffraction pattern of $\text{Ni}_3\text{In}_2\text{Se}_2$ compound. (b) Single crystal x-ray diffraction pattern. (Inset figure illustrate FWHM corresponding (006) plane.) (c) Unit cell of $\text{Ni}_3\text{In}_2\text{Se}_2$. (d) Energy dispersive spectroscopy of $\text{Ni}_3\text{In}_2\text{Se}_2$ single crystal.

tal samples was performed using Rigaku x-ray diffractometer with $\text{Cu-K}\alpha$ $\lambda = 1.54 \text{ \AA}$. Energy dispersive spectra (EDS) were obtained using the FE-SEM model Quanta FEG 250 to assess nominal composition. Measurements of electronic transport, longitudinal resistivity, and Hall resistivity were performed on a freshly cleaved single crystal with typical dimensions of $2 \text{ mm} \times 1.3 \text{ mm} \times 0.21 \text{ mm}$. Measurements utilized conventional linear four-probe and five-probe techniques with the ACT options of the Physical Property Measurement System (PPMS) by Quantum Design Inc. USA. The electronic structure calculations were performed using the Vienna *ab initio* simulation package (VASP) code.^{22–24} The generalized gradient approximations with Perdew-Burke-Ernzerhof (PBE) exchange-correlation functional was employed in the calculations.²⁵ A Γ -centered k-mesh of $15 \times 15 \times 15$ was used for the sampling of the first Brillouin Zone (BZ). The crystal structure was optimized for a force convergence of $10^{-3} \text{ eV}\text{\AA}^{-1}$, an electronic convergence of 10^{-6} eV and a plane wave of cutoff energy of 516 eV respectively, in our calculations. The maximally localized wannier functions, as implemented in wannier90 code²⁶, were utilized to construct the tight binding Hamiltonian. The obtained tight binding Hamiltonian was further used in the wannier_tools package^{26,27} to identify topological nodal line features in the $\text{Ni}_3\text{In}_2\text{Se}_2$ compound.

Figure 1(a) shows the Rietveld refinements (RR) obtained from the x-ray diffraction patterns (XRD) of $\text{Ni}_3\text{In}_2\text{Se}_2$ powder samples. The analysis using Full-Prof software version 2019²⁸ reveals that the crystal structure of the $\text{Ni}_3\text{In}_2\text{Se}_2$ sample is in trigonal phase, belonging to the space group $R\bar{3}m$ (#166). The lattice parameters are determined to be $a = b = 5.43 \text{ \AA}$, and $c = 14.24 \text{ \AA}$, resulting in a cell volume of 362.65 \AA^3 . The XRD pattern for the mechanically exfoliated single crystal planes shows the preferred orientation along the crystallographic c -axis as shown in Fig. 1(b). We estimate the full width half maxima (FWHM) of the most intense peak (006) of the single crystals, as shown in the inset of Fig. 1(b). The obtained FWHM value 0.184° indicates that the crystals is of excellent purity. The conventional cell of $\text{Ni}_3\text{In}_2\text{Se}_2$ is shown in Fig. 1(c), with the crystal structure sequence being In-Se-Ni-In-Se. The results of the EDS analysis are presented in Fig. 1(d), showing the weight percentages of the elements in the sample.

Fig. 2(a) presents longitudinal resistivity (magnetic field, $B \parallel c$ -axis & current $I \parallel ab$ plane of the crystal) as a function of temperature in the range from 2 K to 300 K at $B = 0 \text{ T}$. The observed behavior is metallic-like. $\text{Ni}_3\text{In}_2\text{Se}_2$ single crystals exhibit a resistivity of $1.08 \mu\Omega\text{-cm}$ at zero field at 2 K, slightly higher than the previously reported value for $\text{Ni}_3\text{In}_2\text{S}_2$ single crystals.²⁹ The residual resistivity ratio (RRR) of $\text{Ni}_3\text{In}_2\text{Se}_2$ single crystals, calculated as $(\rho_{xx}(300 \text{ K})) / (\rho_{xx}(2 \text{ K}))$, is determined to be 30, indicating high-quality of grown single crystals. Attempts are made to fit the temperature variation of the resistivity curve with the Bloch-Gruneisen (BG)³⁰ model between temperatures of 2 K and 300 K using the equation.

$$\rho_{xx}(T) = \rho_0 + A \left(\frac{T}{\theta_D} \right)^5 \int_0^{\left(\frac{\theta_D}{T} \right)} \frac{x^5}{(e^x - 1)(1 - e^{-x})} dx \quad (1)$$

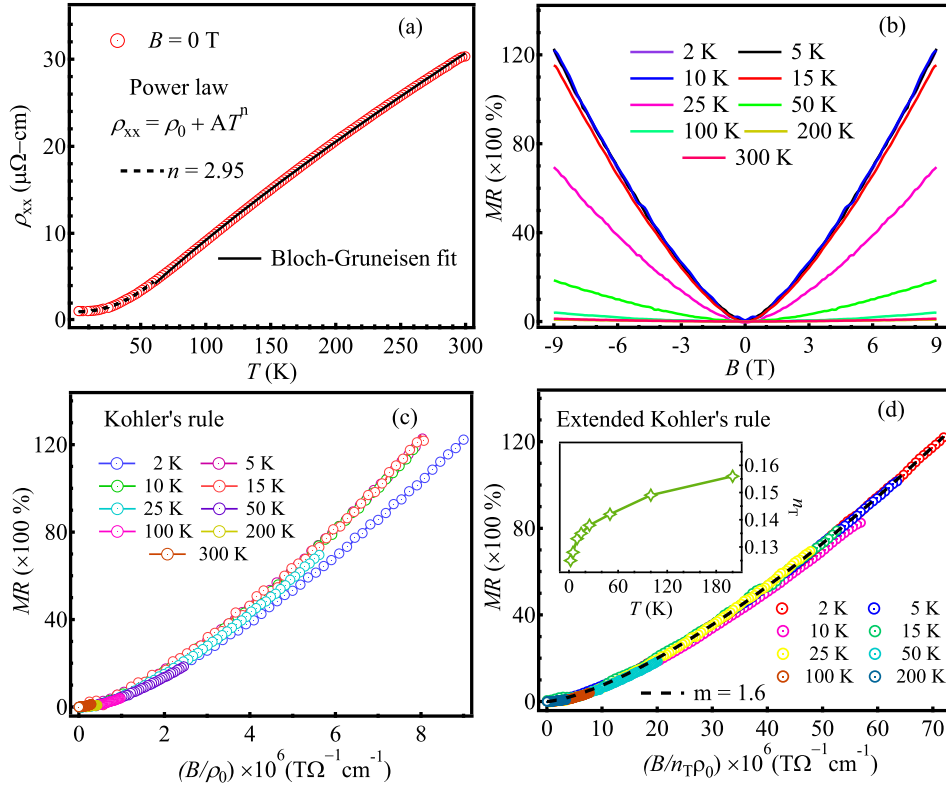


FIG. 2. (a) Longitudinal resistivity (ρ_{xx}) as a function of temperatures (T) at zero magnetic field ($B = 0$ T). The Bloch-Grüneisen fit (50 K to 300 K) is indicated by the solid black line, and the s - d interband scattering ($n = 2.95$) (2 K to 50 K) is represented by the dashed black line. (b) The variation of MR% with magnetic field at different temperatures. (c) Illustrates violation of Kohler's rule analysis of the temperature dependence of the resistivity. (d) Illustrates validation of extended Kohler's rule analysis of the temperature dependence of the resistivity, and inset figure shows variation of density (n_T) with temperature.

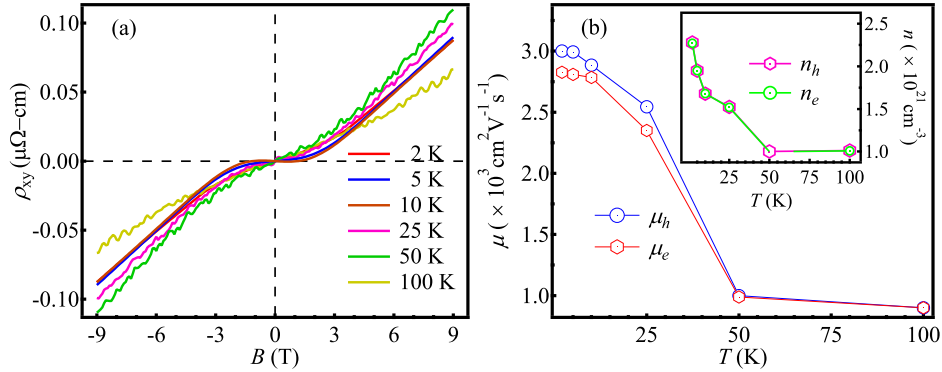


FIG. 3. Hall analysis of $\text{Ni}_3\text{In}_2\text{Se}_2$ single crystal. (a) Hall resistivity (ρ_{xy}) as a function of magnetic field with different temperatures. (b) The carrier mobility of holes and electrons as a function of temperature obtained from two-band model, whereas inset shows the carrier density of holes and electrons with variation of temperature.

where ρ_0 is the residual resistivity A is a constant and θ_D is the Debye temperature. The fitted values are $\rho_0 = 0.478 \mu\Omega\text{-cm}$ and $\theta_D = 75$ K respectively. The model fits well up to 50 K from 300 K, suggesting that in this temperature range, e - p interactions control the scattering. $\rho_{xx}(T)$ data below 50 K is inconsistent with the BG model; therefore, we fitted with a

power law $\rho_{xx}(T) = \rho_0 + AT^n$. The value of the n is close to 3, indicating that the scattering mechanism is influenced by phonon assisted s - d interband scattering³⁰⁻³³, therefore two different types of scattering mechanism are responsible for the evolution of temperature dependent resistivity in the range 2 K to 300 K. The MR of $\text{Ni}_3\text{In}_2\text{Se}_2$ single crystals are stud-

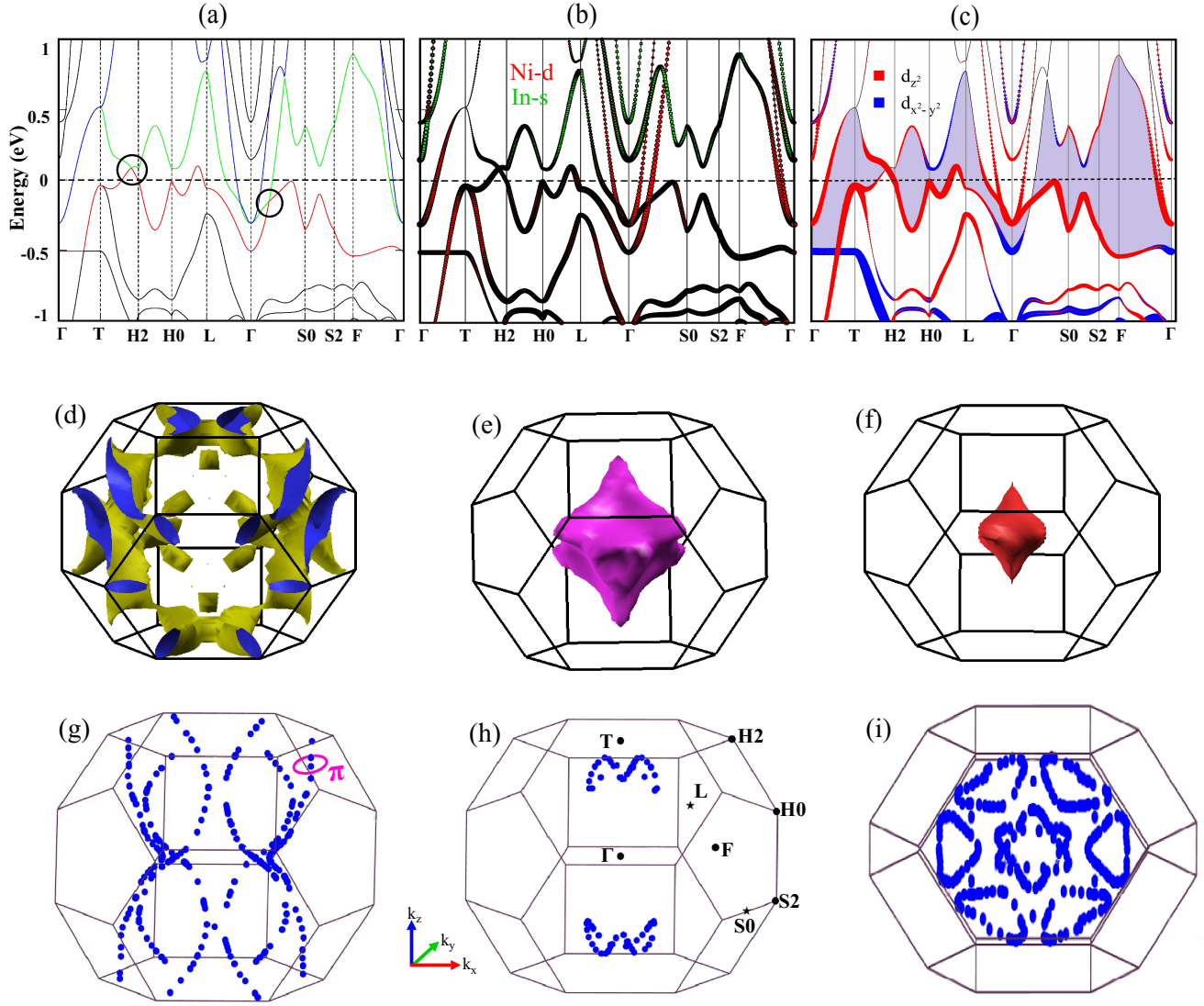


FIG. 4. (a) The electronic band structure of the $\text{Ni}_3\text{In}_2\text{Se}_2$ compound, without SOC; bands crossings near the Fermi level (E_F) are indicated by solid black circles. (b) The character bands for $\text{Ni}_3\text{In}_2\text{Se}_2$ (the red and green colors correspond to Ni-d and In-s orbitals respectively). (c) Illustrates the band structure of Ni 3d orbitals in $\text{Ni}_3\text{In}_2\text{Se}_2$, where the red and blue squares indicate the d_{z^2} and $d_{x^2-y^2}$ respectively. The shaded area indicates the local indirect-type band gap. (d), (e), and (f) display the Fermi surfaces of the $\text{Ni}_3\text{In}_2\text{Se}_2$ compound. (g) Depiction of six endless nodal lines in blue, denoting band crossings in the first Brillouin zone, accompanied by a π -Berry phase. (h) Exhibits two nodal rings within the Brillouin zone. (i) Provides a top-view representation of the nodal lines and nodal rings in the Brillouin zone for the $\text{Ni}_3\text{In}_2\text{Se}_2$ compound.

ied, with $MR = \frac{\rho_{xx}(B) - \rho_{xx}(0)}{\rho_{xx}(0)} \times 100\%$ where $\rho_{xx}(B)$ and $\rho_{xx}(0)$ are the longitudinal resistivities at field B and 0 T, respectively. Fig. 2(b) displays the MR variations with field B at various temperatures. The maximum MR observed is 120% at 2 K and 9 T. However, the MR decreases significantly as the temperature increases. We fit the MR data using Kohler's rule to better understand the role played by multiple scattering mechanisms and the temperature dependency of carriers. Kohler's rule states that in metals and topological or ordinary semimetals, the MR to an applied magnetic field takes the form of a functional parameter (magnetic field divided by

residual resistivity), or $MR = f(B/\rho_0)$.^{32,34,35} The main findings of the MR behavior in $\text{Ni}_3\text{In}_2\text{Se}_2$ are shown in Fig. 2(c) and Fig. 2(d), which demonstrate the violation of Kohler's rule and the validation of the extended Kohler's rule, respectively. The MR curves against B/ρ_0 in Fig. 2(c) do not collapse onto a single curve, indicating a clear violation of Kohler's rule. This is expected since the resistivity versus temperature data exhibit multiple scattering mechanisms, and it's possible that the carrier density varies with temperature. To incorporate temperature-dependent carrier density into Kohler's rule, we introduce a temperature-dependent multiplier $1/n_T$ to

B/ρ_0 on the x -axis of the MR curve, known as the extended Kohler's rule.^{36–40} Fig. 2(d) illustrates that $\text{Ni}_3\text{In}_2\text{Se}_2$ obeys the extended Kohler's rule. Temperature dependence of n_T for single crystal $\text{Ni}_3\text{In}_2\text{Se}_2$ is shown in Fig. 2(d), which was obtained using an extended Kohler's rule³⁶ i.e., $\text{MR} = \alpha(B/n_T\rho_0)^m$; where α and m are being constant parameters and their obtained values are $\alpha = 9.23 \times 10^{-10}$ ($\Omega\text{cm/T}$)^{1.6} and m is 1.6 respectively.

We measured the Hall resistivity (ρ_{xy}) at different temperatures between 2 K and 100 K as a function of magnetic field shown in Fig. 3(a). The non-linear behavior of the Hall resistivity indicates the existence of two different kinds of charge carriers in $\text{Ni}_3\text{In}_2\text{Se}_2$ single crystal. In order to examine this behavior, we used a two-band model to fit ρ_{xy} .⁴¹

$$\rho_{xy} = \frac{B}{e} \frac{(n_h\mu_h^2 - n_e\mu_e^2) + (n_h - n_e)\mu_h^2\mu_e^2B^2}{(n_h\mu_h + n_e\mu_e)^2 + (n_h - n_e)^2\mu_h^2\mu_e^2B^2} \quad (2)$$

where μ_h and μ_e stand for hole and electron mobilities, respectively, and n_h and n_e denote the carrier densities of the holes and electrons, respectively. The hole and electron carrier densities at 2 K are, respectively, $n_h \sim 2.279(1) \times 10^{21} \text{ cm}^{-3}$ and $n_e \sim 2.270(1) \times 10^{21} \text{ cm}^{-3}$, and the hole and electron mobilities are, respectively, $\mu_h \sim 2826 \text{ cm}^2\text{V}^{-1}\text{s}^{-1}$ and $\mu_e \sim 2999 \text{ cm}^2\text{V}^{-1}\text{s}^{-1}$. Between 2 K and 50 K, we saw a strong temperature dependence of $n_{h,e}(T)$ and $\mu_{h,e}(T)$, which might have resulted in a major violation of Kohler's rule in this temperature range.

We now focus our attention onto the first-principles calculations. The conventional BZ is shown in see Supplementary information (SI) Fig. S1(a). The optimized lattice constants are $a = b = 5.44 \text{ \AA}$, and $c = 14.25 \text{ \AA}$, which are in close agreement with that of the experimental parameters. The dynamical stability of the optimized compound is ensured via positive phonon frequencies as shown in Fig. S1(b). The band structure of $\text{Ni}_3\text{In}_2\text{Se}_2$ without the inclusion of the SOC is shown in Fig. 4(a). It is seen from the Fig. 4(a) that there are three bands (shown in red, green and blue colors) that cross Fermi level E_F indicating that the compound is semi-metallic. For the three crossed bands, we have plotted the corresponding three Fermi surfaces as shown in Fig. 4(d), 4(e), and 4(f). The linear band crossings along T-H_2 (around 0.7 eV above E_F) and along $\Gamma\text{-S}_0$ (around -0.156 eV below E_F) are shown in solid circles may give the nodal line behavior in this compound. These band crossings are mainly due to the Ni-d orbitals as can be seen from the character band plot as shown in Fig. 4(b). The three crossed bands give rise to various electron (e) and hole (h) pockets. The red band has electron pocket nature along $\text{H}_2\text{-H}_0$ and $\text{H}_0\text{-}\Gamma$ and hole nature along the T-H_2 and $\text{H}_0\text{-T}$. The green band has electron pocket nature along $\text{L-}\Gamma$ and hole nature along the $\text{H}_2\text{-H}_0$. The blue band has electron pocket nature along Γ and hole nature along the $\Gamma\text{-T}$. Altogether the entire electron and hole pockets gets compensated gives rise to e - h compensation which is also confirmed from electronic transport measurements.

The d_{z^2} and $d_{x^2-y^2}$ orbitals of Ni atom create a local indirect type band gap as shown in Fig. 4(c) around the Fermi level (E_F). The Ni- d_{z^2} orbital possesses electron-like nature and $d_{x^2-y^2}$ has hole-like nature around E_F (see in Fig. 4(c))

and have spherical Fermi surface like nature due to valleys and peak nature. Due to this valley peak nature, the indirect band gap like behavior around E_F , causes the motion of electrons and holes in a fast manner resulting in high mobility and large MR in the $\text{Ni}_3\text{In}_2\text{Se}_2$ compound. The nodal line features of $\text{Ni}_3\text{In}_2\text{Se}_2$ without SOC is shown in 3D BZ as can be seen from Fig. 4(g). From Fig. 4(g) and 4(h), it is clear the $\text{Ni}_3\text{In}_2\text{Se}_2$ compound exhibits six endless Dirac nodal lines and two nodal rings are observed. These nodal lines and nodal rings possesses π -Berry phase as we found that $\frac{1}{2\pi} \oint_{\mathcal{S}} F_n(k) \cdot dS = 1$;⁴² similar kind of endless Dirac nodal lines were observed recently in the isostructural compound $\text{Ni}_3\text{In}_2\text{S}_2$.²⁰ The band structure of $\text{Ni}_3\text{In}_2\text{Se}_2$ with SOC is shown in Fig. S1(c). From Fig. S1(c), it is clearly seen that the nodal line features are destroyed with the application of SOC.

In summary, we have grown high-quality kagome crystals of $\text{Ni}_3\text{In}_2\text{Se}_2$, exhibiting compensated semi-metallic behavior with two distinct scattering mechanisms in the temperature-dependent resistivity data: s - d interband scattering below 50 K and electron-phonon scattering above 50 K. The carrier densities vary with temperature, aligning with the extended Kohler's rule. Magnetoresistance measurements yield 120% MR, while Hall measurements estimate carrier mobility of $\sim 3000 \text{ cm}^2\text{V}^{-1}\text{s}^{-1}$. DFT calculations reveal endless Dirac nodal lines and nodal rings with a π -Berry phase in the $\text{Ni}_3\text{In}_2\text{Se}_2$ crystal. The electronic band structure displays a local indirect-type band gap close to the Fermi level (E_F), formed by peaks and valleys of the hole-like $d_{x^2-y^2}$ and electron-like d_{z^2} orbitals of the Ni atom. The observed high carrier mobilities and comparatively high MR result from electrons and holes moving faster through these peaks and valleys.

ACKNOWLEDGMENTS

P. Das acknowledge UGC-DAE CSR, Indore center for the financial support through the project Ref. No. CRS/2021-22/01/425. The authors of GGv are acknowledging DST, Government of India for supporting the Department of Pure and Applied Physics through FIST Level-I program. We also acknowledges UGC-DAE CSR, Indore for electronic transport measurements using the PPMS.

CONFLICT OF INTEREST

The authors have no conflicts to disclose.

DATA AVAILABILITY STATEMENT

The data are available from the corresponding author upon reasonable request.

¹K. Sun, Z. Gu, H. Katsura, and S. D. Sarma, Physical review letters **106**, 236803 (2011).

- ²D. Sheng, Z.-C. Gu, K. Sun, and L. Sheng, *Nature communications* **2**, 389 (2011).
- ³T. Neupert, L. Santos, C. Chamon, and C. Mudry, *Physical review letters* **106**, 236804 (2011).
- ⁴E. Tang, J.-W. Mei, and X.-G. Wen, *Physical review letters* **106**, 236802 (2011).
- ⁵Z. Guguchia, J. Vezhzhak, D. Gawryluk, S. Tsirkin, J.-X. Yin, I. Belopolski, H. Zhou, G. Simutis, S.-S. Zhang, T. Cochran, G. Chang, E. Pomjakushina, L. Keller, Z. Skrzeczkowska, Q. Wang, H. C. Lei, R. Khasanov, A. Amato, S. Jia, T. Neupert, H. Luetkens, and M. Z. Hasan, *Nature communications* **11**, 559 (2020).
- ⁶J.-X. Yin, S. S. Zhang, H. Li, K. Jiang, G. Chang, B. Zhang, B. Lian, C. Xiang, I. Belopolski, H. Zheng, T. Cochran, S.-Y. Xu, G. Bian, K. Liu, T. R. Chang, H. Lin, Z.-Y. Lu, Z. Wang, S. Jia, W. Wang, and M. Z. Hasan, *Nature* **562**, 91–95 (2018).
- ⁷L. Ye, M. Kang, J. Liu, F. Von Cube, C. R. Wicker, T. Suzuki, C. Jozwiak, A. Bostwick, E. Rotenberg, D. C. Bell, L. Fu, R. Comin, and J. G. Checkelsky, *Nature* **555**, 638–642 (2018).
- ⁸B. Sales, W. Meier, A. May, J. Xing, J.-Q. Yan, S. Gao, Y. Liu, M. Stone, A. Christianson, Q. Zhang, and M. A. McGuire, *Physical Review Materials* **5**, 044202 (2021).
- ⁹C. Fang, H. Weng, X. Dai, and Z. Fang, *Chinese Physics B* **25**, 117106 (2016).
- ¹⁰M. Li, Q. Wang, G. Wang, Z. Yuan, W. Song, R. Lou, Z. Liu, Y. Huang, Z. Liu, H. Lei, Z. Yin, and S. Wang, *Nature communications* **12**, 3129 (2021).
- ¹¹P. Mendels and F. Bert, *Comptes Rendus Physique* **17**, 455–470 (2016).
- ¹²D. Liu, A. Liang, E. Liu, Q. Xu, Y. Li, C. Chen, D. Pei, W. Shi, S. Mo, P. Dudin, T. Kim, C. Cacho, G. Li, Y. Sun, L. X. Yang, Z. K. Liu, S. S. P. Parkin, C. Felser, and Y. L. Chen, *Science* **365**, 1282–1285 (2019).
- ¹³M. A. Kassem, Y. Tabata, T. Waki, and H. Nakamura, *Journal of Crystal Growth* **426**, 208–213 (2015).
- ¹⁴L. Jiao, Q. Xu, Y. Cheon, Y. Sun, C. Felser, E. Liu, and S. Wirth, *Physical Review B* **99**, 245158 (2019).
- ¹⁵M. Kanagaraj, J. Ning, and L. He, *Reviews in Physics* **8**, 100072 (2022).
- ¹⁶M. Tanaka, Y. Fujishiro, M. Mogi, Y. Kaneko, T. Yokosawa, N. Kanazawa, S. Minami, T. Koretsune, R. Arita, S. Tarucha, M. Yamamoto, and Y. Tokura, *Nano Letters* **20**, 7476–7481 (2020).
- ¹⁷E. Liu, Y. Sun, N. Kumar, L. Muechler, A. Sun, L. Jiao, S.-Y. Yang, D. Liu, A. Liang, Q. Xu, V. Süß, H. Borrmann, C. Shekhar, Z. Wang, W. Xi, Chuanying and Wang, W. Schnelle, S. Wirth, Y. Chen, S. T. B. Goennenwein, and C. Felser, *Nature physics* **14**, 1125–1131 (2018).
- ¹⁸Y. Okamura, S. Minami, Y. Kato, Y. Fujishiro, Y. Kaneko, J. Ikeda, J. Muramoto, R. Kaneko, K. Ueda, V. Kocsis, N. Kanazawa, Y. Taguchi, T. Koretsune, K. Fujiwara, A. Tsukazaki, R. Arita, Y. Tokura, and Y. Takahashi, *Nature communications* **11**, 4619 (2020).
- ¹⁹A. R. Karmakar, S. Nandy, A. Taraphder, and G. P. Das, *Physical Review B* **106**, 245133 (2022).
- ²⁰T. Zhang, T. Yilmaz, E. Vescovo, H. Li, R. G. Moore, H. N. Lee, H. Miao, S. Murakami, and M. A. McGuire, *npj Computational Materials* **8**, 155 (2022).
- ²¹L. Cao, G. Liu, Y. Zhang, Z. Yu, Y.-Y. Lv, S.-H. Yao, J. Zhou, Y. Chen, and Y.-F. Chen, *Physical Review Materials* **7**, 084203 (2023).
- ²²P. Hohenberg and W. Kohn, *Physical review* **136**, B864 (1964).
- ²³G. Kresse and J. Furthmüller, *Physical review B* **54**, 11169 (1996).
- ²⁴G. Kresse and J. Furthmüller, *Computational materials science* **6**, 15–50 (1996).
- ²⁵J. P. Perdew, K. Burke, and M. Ernzerhof, *Physical review letters* **77**, 3865 (1996).
- ²⁶N. Marzari and D. Vanderbilt, *Physical review B* **56**, 12847 (1997).
- ²⁷Q. Wu, S. Zhang, H.-F. Song, M. Troyer, and A. A. Soluyanov, *Computer Physics Communications* **224**, 405–416 (2018).
- ²⁸J. Rodríguez-Carvajal, “An introduction to the program,” Full prof (2000).
- ²⁹H. Fang, M. Lyu, H. Su, J. Yuan, Y. Li, L. Xu, S. Liu, L. Wei, X. Liu, H. Yang, Q. Yao, M. Wang, Y. Guo, W. Shi, Y. Chen, E. Liu, and Z. Liu, *Science China Materials* **66**, 1–7 (2023).
- ³⁰J. Ziman, “Electrons and phonons (clarendon press, oxford),” (1960).
- ³¹Z. Hu, Q. Du, Y. Liu, D. Graf, and C. Petrovic, *Applied Physics Letters* **117** (2020).
- ³²Y. Wang, L. Thoutam, Z. Xiao, J. Hu, S. Das, Z. Mao, J. Wei, R. Divan, A. Luican-Mayer, G. Crabtree, and W. K. Kwok, *Physical Review B* **92**, 180402 (2015).
- ³³C. Shekhar, A. K. Nayak, Y. Sun, M. Schmidt, M. Nicklas, I. Leermakers, U. Zeitler, Y. Skourski, J. Wosnitza, Z. Liu, Y. Chen, W. Schnelle, H. Borrmann, Y. Grin, C. Felser, and B. Yan, *Nature Physics* **11**, 645–649 (2015).
- ³⁴M. Kohler, *Annalen der Physik* **424**, 211–218 (1938).
- ³⁵A. Narayanan, M. Watson, S. Blake, N. Bruyant, L. Drigo, Y. Chen, D. Prabhakaran, B. Yan, C. Felser, T. Kong, P. C. Canfield, and A. Coldea, *Physical Review Letters* **114**, 117201 (2015).
- ³⁶J. Xu, F. Han, T.-T. Wang, L. R. Thoutam, S. E. Pate, M. Li, X. Zhang, Y.-L. Wang, R. Fotovat, U. Welp, X. Zhou, W.-K. Kwok, D. Y. Chung, M. G. Kanatzidis, and Z.-L. Xiao, *Physical Review X* **11**, 041029 (2021).
- ³⁷A. Wang, D. Graf, Y. Liu, Q. Du, J. Zheng, H. Lei, and C. Petrovic, *Physical Review B* **96**, 121107 (2017).
- ³⁸R. Sankar, G. Peramaiyan, I. P. Muthuselvam, S. Xu, M. Z. Hasan, and F. Chou, *Journal of Physics: Condensed Matter* **30**, 015803 (2017).
- ³⁹I. A. Leahy, Y.-P. Lin, P. E. Siegfried, A. C. Treglia, J. C. Song, R. M. Nandkishore, and M. Lee, *Proceedings of the National Academy of Sciences* **115**, 10570–10575 (2018).
- ⁴⁰N. Karn, M. Sharma, and V. Awana, *Journal of Applied Physics* **133** (2023).
- ⁴¹D. Shoenberg, *Magnetic oscillations in metals* (Cambridge university press, 2009).
- ⁴²S. A. H. Gangaraj, M. G. Silveirinha, and G. W. Hanson, *IEEE journal on multiscale and multiphysics computational techniques* **2**, 3–17 (2017).